Fuel 288 (2021) 119607

Contents lists available at ScienceDirect

Fuel

journal homepage: www.elsevier.com/locate/fuel

Full Length Article

Experimental investigations on the chlorine-induced corrosion of HVOF thermal sprayed Stellite-6 and NiAl coatings with fluidised bed biomass/anthracite combustion systems

Hetian Chi [a,b], Miguel A. Pans [a,1], Mingwen Bai [a,2], Chenggong Sun [a], Tanvir Hussain [a], Wei Sun [a], Yuge Yao [c], Junfu Lyu [c], Hao Liu [a,*]

[a] Faculty of Engineering, University of Nottingham, University Park, Nottingham NG7 2RD, UK
[b] Economy & Technology Research Institute, State Grid Hubei Electric Power Company, Wuhan 430077, China
[c] Department of Energy and Power Engineering, Tsinghua University, Beijing 100084, China

ARTICLE INFO

Keywords:
Stellite-6
NiAl
High-velocity oxy fuel (HVOF)
High-temperature corrosion
Bubbling fluidised bed (BFB)
Circulating fluidised bed (CFB)

ABSTRACT

Stellite-6 (Co-based) and NiAl coatings (Ni-based) were deposited via HVOF spraying onto 304 stainless steels and tested in a 20 kW_{th} biomass fired bubbling fluidised bed (BFB) combustor for 20 h and an industrial scale anthracite fired CFB boiler for 1630 h. Stellite-6 showed excellent corrosion resistance in both fluidised bed combustion systems because of the formation of the outermost Cr_2O_3 layer and the spinel $CoCr_2O_4$ beneath, whereas NiAl coatings' anti-corrosion performance was significantly depleted due to the chlorine attack, and the resultant formation of Al_2O_3 layer at the coating/substrate interface finally led to coating spallation in both systems.

1. Introduction

To prevent the severe impacts of climate change, the European Union (EU) has set ambitious targets for the energy sectors, including raising the renewable energy source consumption to 35% by 2030 [1]. Currently, bioenergy contributes over two-thirds to the total renewable energy supply [2] and is expected to further increase by 2030 [3]. This amount of bioenergy mainly comes from biomass combustion power plants firing wood (pellets) given their benefits of high energy density and particularly low ash content [3]. However, the increasing demand for woody biomass in the energy industry will inevitably lead to a price rise for quality woody biomass and the call for an increase in the utilisation of other kinds of biomass fuels such as agricultural crop residues, by-products and wastes to meet the ambitious EU goals [4]. However, non-woody biomass fuels impose greater challenges to current solid fuel combustion boilers as they normally have a higher content of ash which is rich in alkali metals, chlorine and other corrosive elementals [5] that are the precursors of the well-established corrosion mechanism of "active oxidation" [6]. Meanwhile, the worldwide interests of higher energy efficiency and CO_2 capture and utilisation have motivated the development, demonstration and commercialisation of ultra-supercritical (USC) circulating fluidised bed (CFB) solid fuel combustion power plants [7]. These emerging USC-CFB boiler technologies are particularly suitable for the combustion of non-woody biomass fuels due to their great fuel flexibility [8]. However, the fireside corrosion resistance of the conventional CFB boiler tube materials may not be good enough to withstand the harsh combustion conditions (e.g. rather high local temperatures within the range of about 400–800 °C with random bed material collisions) within a USC-CFB boiler [9].

Thermal spray methods, especially high velocity oxy-fuel (HVOF) thermal spraying, have been widely used to produce various corrosion resistant coatings in the past. The HVOF spraying is a thermal coating process involving the delivery of coating powder axially, into a pre-ignited mixture of oxygen and fuel, ejected through a nozzle. The material is then propelled at supersonic velocity toward the surface to be coated. The HVOF thermal sprayed coatings have shown great corrosion resistance in the high temperature range because of their low porosity and high adhesion [10–12]. From the perspective of corrosion and

* Corresponding author at: Department of Architecture and Built Environment, Faculty of Engineering, University of Nottingham, University Park, Nottingham NG7 2RD, UK.
E-mail address: Liu.Hao@nottingham.ac.uk (H. Liu).
[1] Current affiliation: Centre for Renewable Energy Systems Technology, Loughborough University, Loughborough LE11 3TU, UK.
[2] Current affiliation: Institute for Future Transport & Cities, Coventry University, Coventry, CV1 5FB, UK.

https://doi.org/10.1016/j.fuel.2020.119607
Received 7 May 2020; Received in revised form 29 September 2020; Accepted 23 October 2020
Available online 19 November 2020
0016-2361/© 2020 The Author(s). Published by Elsevier Ltd. This is an open access article under the CC BY license (http://creativecommons.org/licenses/by/4.0/).

oxidation resistance, iron or nickel alloying with over 25 wt% chromium could provide great improvement by forming Cr_2O_3 protective scales as an outer layer [13,14]. Moreover, the HVOF sprayed Stellite-6 coating (Co-Cr-W-C) has been demonstrated as one of the best corrosion protection methods in pulverised coal firing boilers at the superheaters under an average temperature of 900 °C given the formation of the spinel $CoCr_2O_4$ at the outermost layer [15]. When it comes to biomass combustion, further concerns were raised against the protective Cr_2O_3 forming alloys as the alkali chlorides could react with Cr_2O_3 forming K_2CrO_4 which facilitated the chlorine penetration and led to continuous corrosion attack across the coating [16–18]. Al_2O_3 forming alloys (Fe-based) were investigated as alternatives at a lower temperature range of 600 °C −700 °C [19,20]. The formation of K_2CrO_4 was hindered by the thermodynamically preferable reaction of producing potassium aluminate [21]. Maria et al. [22] also reported the excellent corrosion resistance of the nickel-based HVOF coatings (NiCr16Mo, NiCr9Mo and NiCr10Al) in a biomass CFB boiler at various temperature level under 800 °C. There was also a study that demonstrated Ni-Al model alloy as a better performer in anti-corrosion comparing to Fe-Cr and Fe-Al at 670 °C under alkali chlorides deposits attack [23]. Bai et al. [24] further studied the corrosion resistance of NiAl coating at 700 °C in a lab-scale environment using HCl synthetic gas with KCl deposits. The results confirmed the protectiveness of the NiAl coating but the impact of the Al_2O_3 formation at the coating/substrate interface remained unclear when applying to fluidised bed combustion systems. Nevertheless, these conclusions were derived from lab-scale isothermal testing results and their verification in real fluidised bed systems is yet to be completed.

In this study, Stellite-6 and NiAl coatings were HVOF thermal sprayed onto 304 stainless steels and installed in a 20kW$_{th}$ biomass-fired bubbling fluidised bed (BFB) combustor, and an industrial anthracite fired CFB boiler. Both systems were controlled at high-end operation bed temperatures (800 °C −900 °C) which can emphasise the corrosion development on the 304 SS and highlight the anti-corrosion abilities of the coatings. Previous studies have shown that 304 SS has little or no resistance against KCl induced corrosion at temperatures above 600 °C [16]. The use of Stellite-6 as coating was according to its outstanding corrosion resistance which had been demonstrated in a wood-fired CFB and a coal-fired pressurised fluidised bed power plant under a maximum temperature of 630 °C [25]. However, at a higher local temperature above 800 °C, the corrosion resistance of the Stellite-6 has not been verified. NiAl coating was investigated in our previous study [24], showing good performances in abating the chlorine induced corrosion under static laboratory environments. A comparison of this coating to the well-established Co-based Stellite-6 is of great importance for potential future implementations in practical fluidised combustion boilers including the most advanced USC-CFB coal/biomass combustion boilers [26]. The corrosion products were analysed by X-ray diffraction (XRD) and Scanning electron microscopy with energy dispersive X-ray spectroscopy (SEM/EDX), in comparison with the corrosion of the plain 304 stainless steel. Possible oxidation and corrosion mechanisms were discussed.

2. Experimental

2.1. Coating materials and substrate

Stellite-6 (nominal composition Co-28.3Cr-4.8W-2.2Ni-1.5Fe-1.2Si-1.2C wt%, Kennametal Inc., UK) and NiAl (nominal composition Ni69Al31 wt%, AMPERIT291, fused/crushed, H.C.Starck Inc., UK) powders were chosen as the feedstock for the liquid fuel based HVOF thermal spray (Metjet IV, Metallisation Ltd., UK) on the AISI 304 stainless steel substrates. The substrates (nominal composition Fe-19.0Cr-9.3Ni-2.0Mn-0.05C wt%; dimension 60*25*2 mm) were grit blasted with brown alumina and cleaned in an ultrasonic acetone bath before coating. The detailed spray coating process was described in our previous studies [24,27]. In general, the setup of the HVOF thermal spray gun was identical in both cases using a 100 mm nozzle and a stand-off distance of 356 mm. However, due to the lower flowability of the NiAl powders, the flow rates of kerosene and oxygen were controlled at 415 mL/min and 800 L/min respectively which were slightly lower than those used for the Stellite-6, i.e. 476 mL/min and 920 L/min for the kerosene and oxygen flow rates. In all cases, optimized spraying parameters, which were developed for commercial applications by the powder suppliers H.C.Starck, Inc. and Kennametal Inc., were used to produce the coatings for this study. Moreover, the NiAl coating experienced 16 passes resulting in a thickness of ~ 250 μm while the Stellite-6 coating was done within 8 passes forming the thickness of ~ 250 μm.

Table 1
Characterisation of the biomass fuels and bed materials (quartz sand).

	MC[c]	WS[d]	Anthracite	Quartz sand
Proximate (wt%)				
Moisture (ar [a])	5.12	13.11	9.17	–
Ash (db [b])	2.09	8.00	41.08	–
Volatile matter (db)	80.19	71.82	17.31	–
Fixed carbon (db)	17.72	20.18	41.61	–
Ultimate (wt%, db)				
Carbon	46.09	43.37	42.76	–
Hydrogen	6.48	6.40	2.80	–
Nitrogen	0.39	0.71	0.65	–
Sulphur	0.09	0.11	0.32	–
Oxygen (by difference)	44.86	41.41	12.39	–
Fuel ash main components (% wt)				
SiO_2	36.40	66.57	34.12	96.67
K_2O	20.40	9.90	1.01	0.01
CaO	5.72	4.85	4.34	0.01
P_2O_5	4.92	1.88	–	–
SO_3	2.72	1.42	0.48	–
MgO	2.00	2.29	1.14	<0.01
Na_2O	1.10	0.28	4.12	0.03
Cl	0.85	0.90	0.79	–
Fe_2O_3	0.34	1.24	17.70	2.40
Al_2O_3	0.00	1.26	33.70	0.33
Ash fusion temperature (°C)				
Deformation temperature	780	798	1320	
Softening temperature	917	1029	1435	
Hemispherical temperature	1092	1323	–	
Flow temperature	1162	1358	–	

[a] As received; [b] Dry base; [c] MC-Miscanthus; [d]WS-Wheat Straw.

2.2. Coating materials tests in the 20kWth bubbling fluidised bed combustor

2.2.1. Fuels and bed material

The fuels used in this study were wheat straw and miscanthus as mentioned in our previous study [28]. In virtue of the inherent high potassium and chlorine contents, the fuel ash can be retained in the bed to form severe bed agglomeration, and the fly ash in the freeboard zone can cause corrosion, slagging and fouling issues. Quartz sand (Garside 14/25) was used as the bed material during all the tests with an initial static bed height of 25 cm. The fuel and bed sand characteristics are shown in Table 1.

2.2.2. Coating materials mounting mechanism

The details of the lab-scale BFB combustor (Fig. 1a) will not be elaborated herein, which were presented in our previous studies [28,29]. Further information on the design and operational conditions of the BFB combustor is provided in Appendix (Fig. A1). In this study, both wheat straw and miscanthus were used as the fuels to create a similar temperature profile across the combustor, i.e. ~ 890 °C at the lower coating materials installation position and ~ 840 °C at the higher mounting position (Fig. 1a). The main reason of choosing these two fuels was because of their large availability in the UK non-woody biomass market. In addition, both fuels are rich in KCl (Fig. 2) which can create a corrosive atmosphere for the anti-corrosion tests of the coating

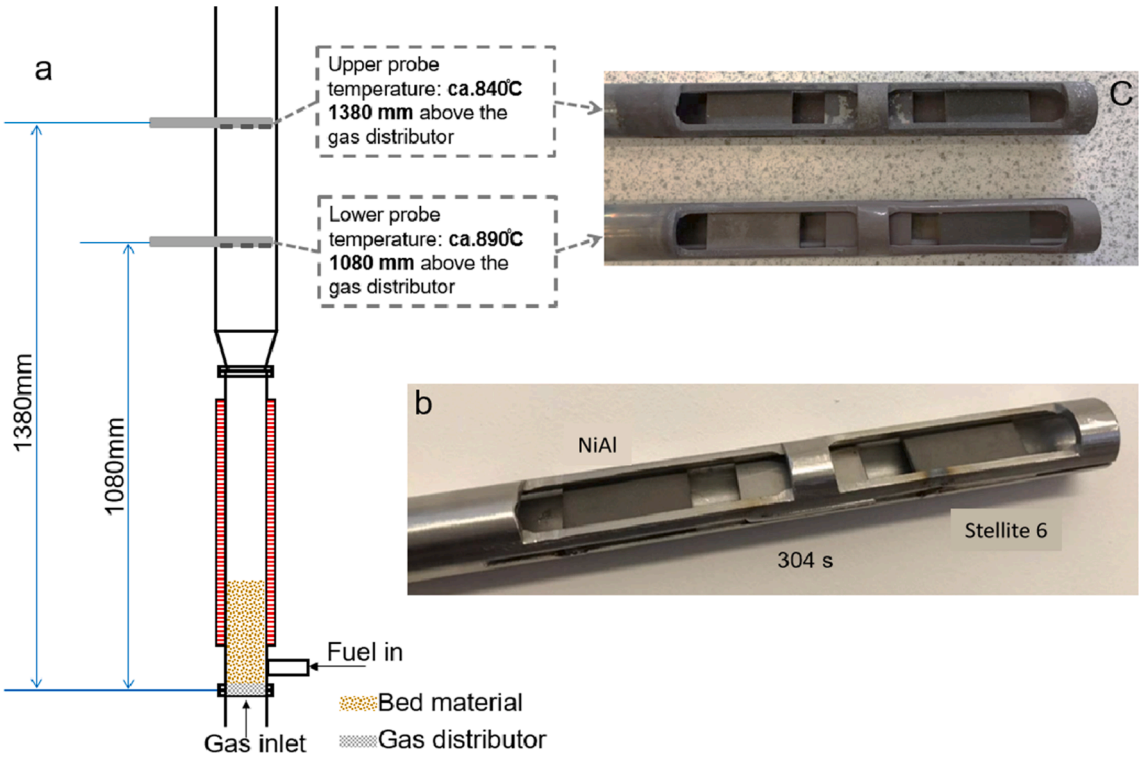

Fig. 1. Simplified schematics of the 20kWth BFB with the coating material probes installation mechanism: a) Coating material probes mounting positions in the 20kWth BFB combustor; b) Coating materials installation in a 310 stainless steel probe; c) The two coating sample probes after tests.

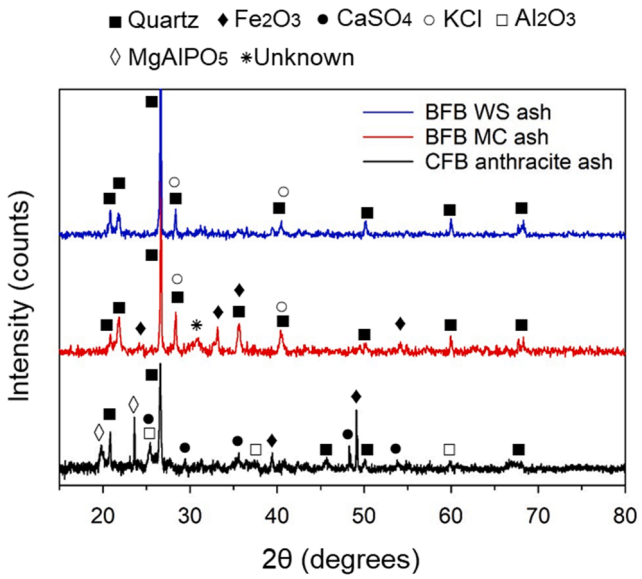

Fig. 2. XRD patterns of the cyclone ash collected in the BFB and CFB experimental systems.

materials. Meanwhile, using different fuels in the BFB setup corresponds to the fact that the industrial biomass-fired BFB boilers commonly consume varieties of biomass fuels.

Fig. 1b shows the mounting mechanism of the coating materials which were welded inside a 310 stainless steel tube (o.d. 19 mm; i.d. 14 mm) with the "window" width of 12 mm. The NiAl and Stellite-6 coating specimens were located symmetrically aside by the 304 SS substrate. Two identical sets of the coating material probes were prepared and inserted into the freeboard zone of the 20kWth BFB combustor facing towards the upcoming fluidisation gas stream. After 20 h high temperature test, the two probes (Fig. 1c) were taken out for further characterisation.

2.3. Coating material tests in the industrial CFB

2.3.1. Fuel and bed material

Anthracite was used as the fuel for the industrial CFB boiler tests. The particle size of the fuel was in the range between 0 and 10 mm with a roughness: D50 = 1.5 mm. The characteristics of the fuel are also shown in Table 1, and the main ash components are shown in Fig. 2. Local sand with a particle size between 0 and 3 mm was used as the bed material.

2.3.2. Coating materials mounting mechanism

The same coating materials tested in the 20 kWth BFB were also installed in an industrial-scale CFB boiler (Fig. 3a) owned by Qinhuangdao Lihua Starch Co.Ltd (Model: TG-180/5.29-M). The boiler has a furnace of 9330 mm width, 5030 mm depth and 36500 mm elevation height. The designed fuel consumption rate is 37740 kg/h. On the steam side, the rated evaporation capacity is $1.8*10^5$ kg/h at 485 °C under 5.3 MPa. During the period of this study, the evaporation capacity was controlled at $1.3*10^5$ kg/h.

The coating materials were welded on the thermocouple probes and inserted into the boiler at the 5 m and 8 m operational platforms facing towards the upcoming fluidisation gas flow (Fig. 3b). Worth noting that the actual height to ground of the lower probe is 5.5 m and hereinafter, 5 m platform is used for simplicity. The average local temperatures were about 840 °C and 860 °C for the 5 m and 8 m installation positions, respectively, during the test. The measurement campaign lasts ca.1630 h based on the power plant scheduled shut down program. After the test campaign, the samples (Fig. 3c) were retrieved for further analysis and characterisation.

2.4. Coating materials characterisation

The coating surfaces and cross-sections were examined by a scanning

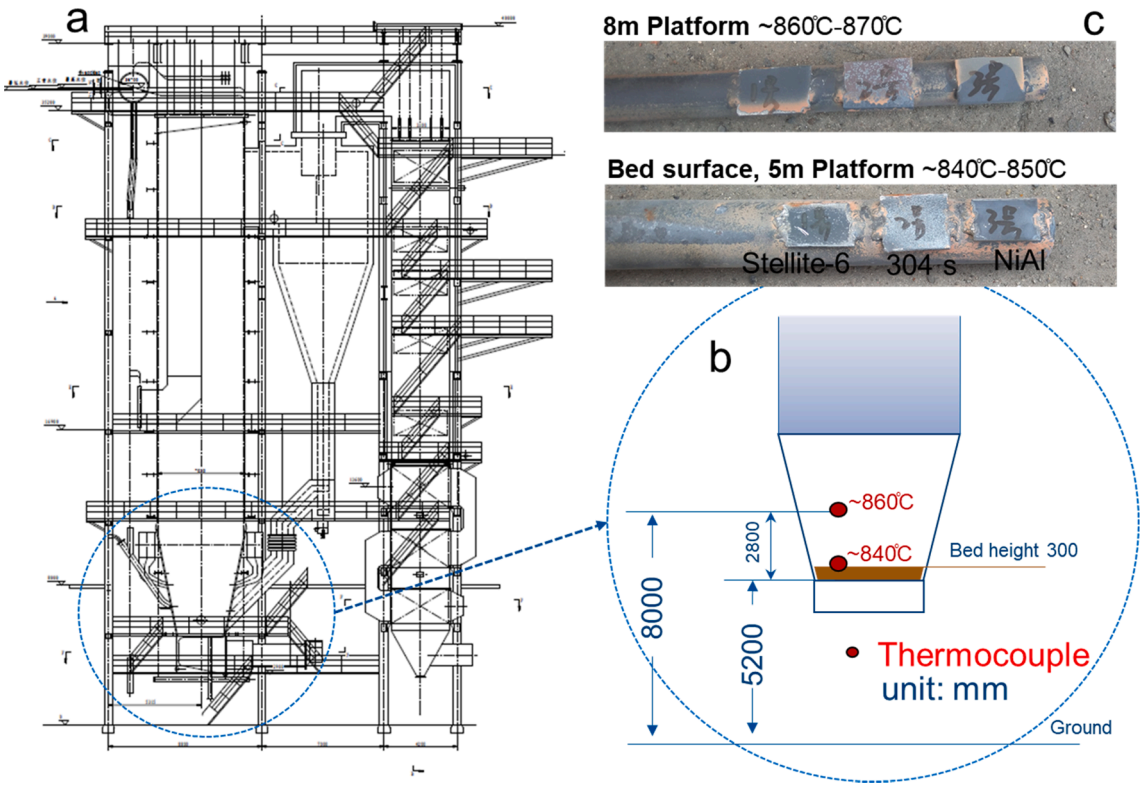

Fig. 3. Schematics of the industrial CFB in Qinhuangdao Lihua Starch Co., Ltd with the coating materials installation mechanism: a) The schematics of the CFB boiler; b) Details of the coating samples installation position; c) Photos of the two thermocouples with welded coating samples after tests.

Table 2
Photograph of the twelve samples after corrosion tests.

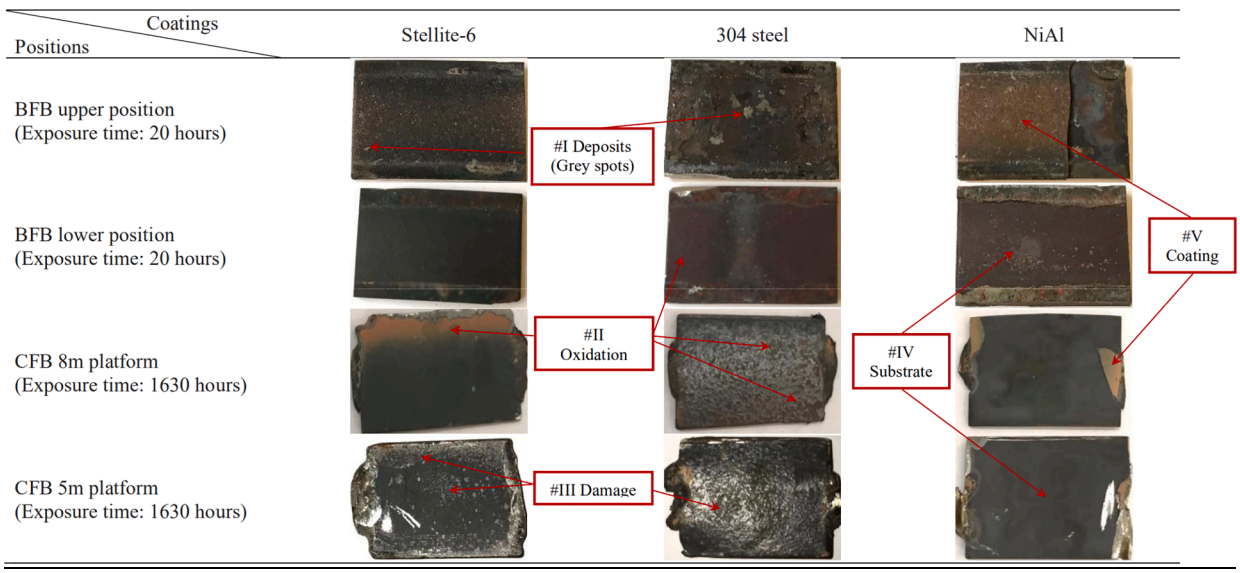

electron microscope (SEM, FEI Quanta 600, UK) under a 20 kV back-scattered electron (BSE) mode and the elemental mapping was conducted with the integrated energy dispersive X-ray (EDX) detector. ESPRIT software (Bruker, Germany) was used to acquire the elemental mapping images which were further edited with Image J for a better presentation of the montages. For the surface morphology, the coating samples were coated with 10 nm carbon considering the formation of sintered ash on the surface. For the cross-section analysis, the coating samples were mounted in cold-mounting resin (EpoFix, Struers, Denmark) and polished sequentially down to a 1 μm diamond finish using a non-aqueous white sprit. The X-ray diffraction (XRD) analysis of the corroded surfaces was conducted by the Bruker D8 Advance Da Vinci system (Germany) using CuKα radiation with Bragg-Brentano set-up in the 2θ range between 20°-90° with a step size of 0.05° and dwell time of 0.2 s. Besides, the XRD analysis was conducted on the fuel ashes to characterise the ash components and the results are shown in Fig. 2. The PDF card numbers of the detected phases are shown in Appendix (Table A.1). In addition, thermodynamic calculations for certain

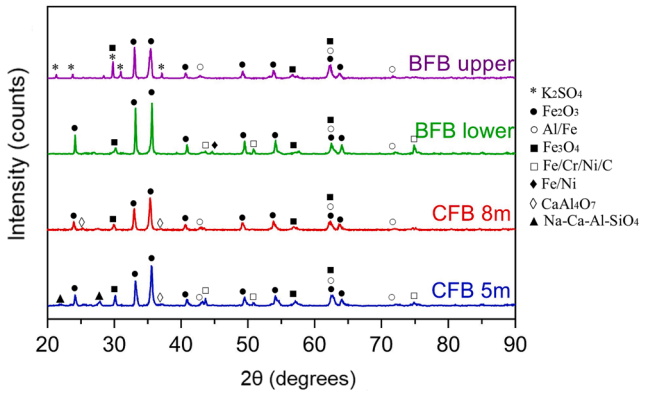

Fig. 4. XRD patterns of the plain 304 stainless steel sample surfaces after the test.

chemical reactions were carried out using the commercially available Thermo-Calc® software (Version 2018b) with SSUB5 (SGTE Substances Database V5.2) following the CALPHAD technique.

3. Results and discussion

3.1. General visual observation

The photos of the retrieved coating samples are listed in Table 2.

Regarding the Stellite-6 coating, there were no obvious changes on the surface when placed at the BFB lower position, but a few ash deposits (*#I*, Table 2) could be observed from the sample located at the BFB upper position. Oxidation (*#II*) could be found on the edge of the Stellite-6 sample at the CFB 8 m platform while the coating was damaged (*#III*) at the 5 m platform exposing the substrates at certain spots. This difference was mainly caused by the collision of the bed materials. At the lower position, the coating was dominantly attacked by the fluidising bed materials and the ash deposits could be easily brushed off. At the higher position, a higher concentration of fly ash was present due to the completion of the fuel combustion, and thus leading to further ash deposits on the samples surfaces. Similar observations could be found on the plain 304 SS substrates. When it comes to the NiAl coatings, it could be seen that the coatings were fully spalled off and exposing the substrates (*#IV*) at the lower position in both setups, while at the higher position, the NiAl coatings were partially spalled off (*#V*). Further characterisation is needed to verify the spall off mechanisms. Moreover, unlike the rough surfaces of the CFB Stellite-6 and 304 SS samples damaged by the bed collision, no clear damages were observed on the CFB NiAl samples after the coating spallation. Meanwhile, surface oxidisation alongside with ash deposits could be spotted on the NiAl coating base layer of the samples from the BFB exposure tests. This indicates the alkali-rich biomass fuels can lead to severer corrosion to the coating layer even within a much shorter exposure time comparing to the anthracite used in the CFB plant.

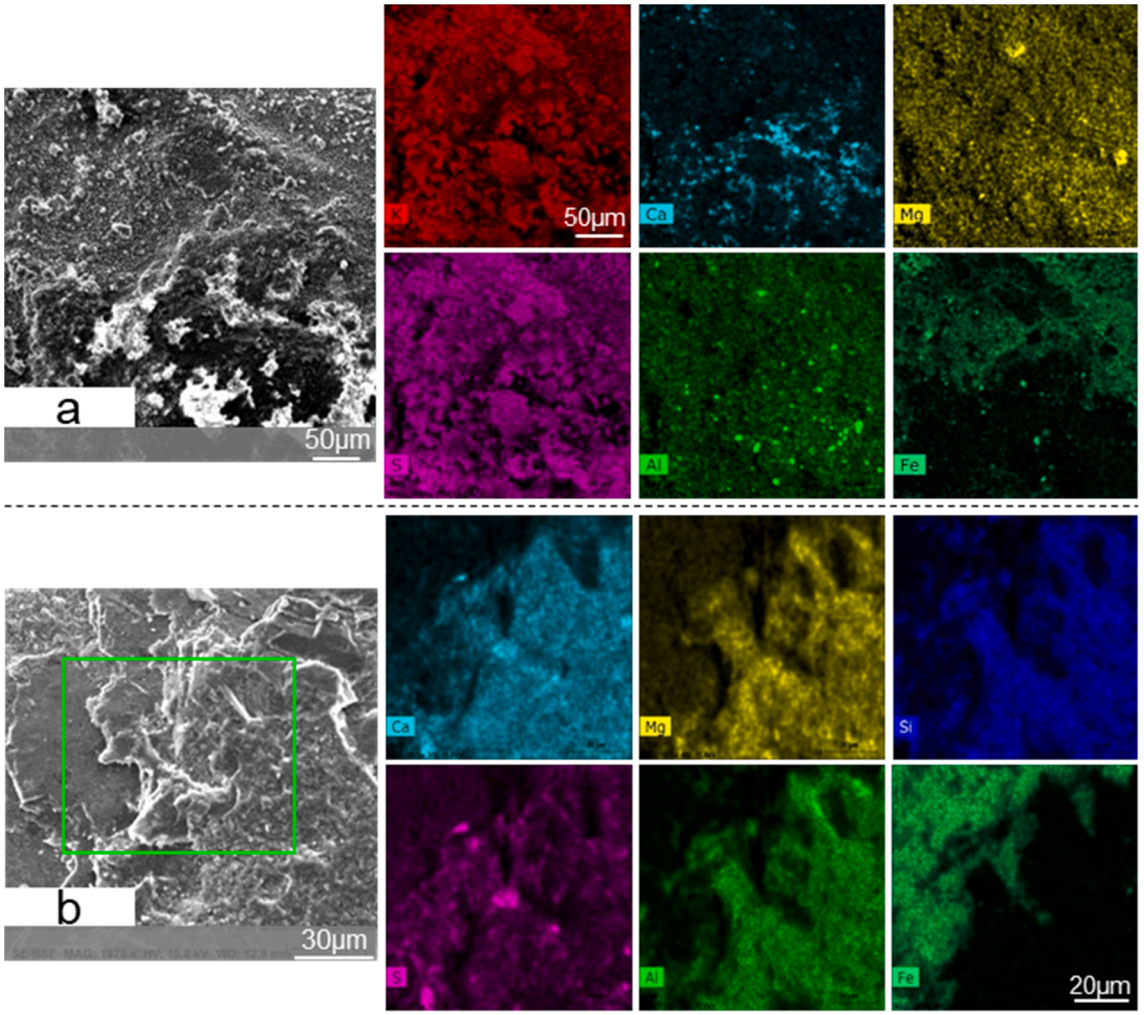

Fig. 5. SEM/EDX elemental mapping on the coating surface after 10 nm carbon coating: a) BFB upper 304 SS; b) CFB 8 m 304 SS.

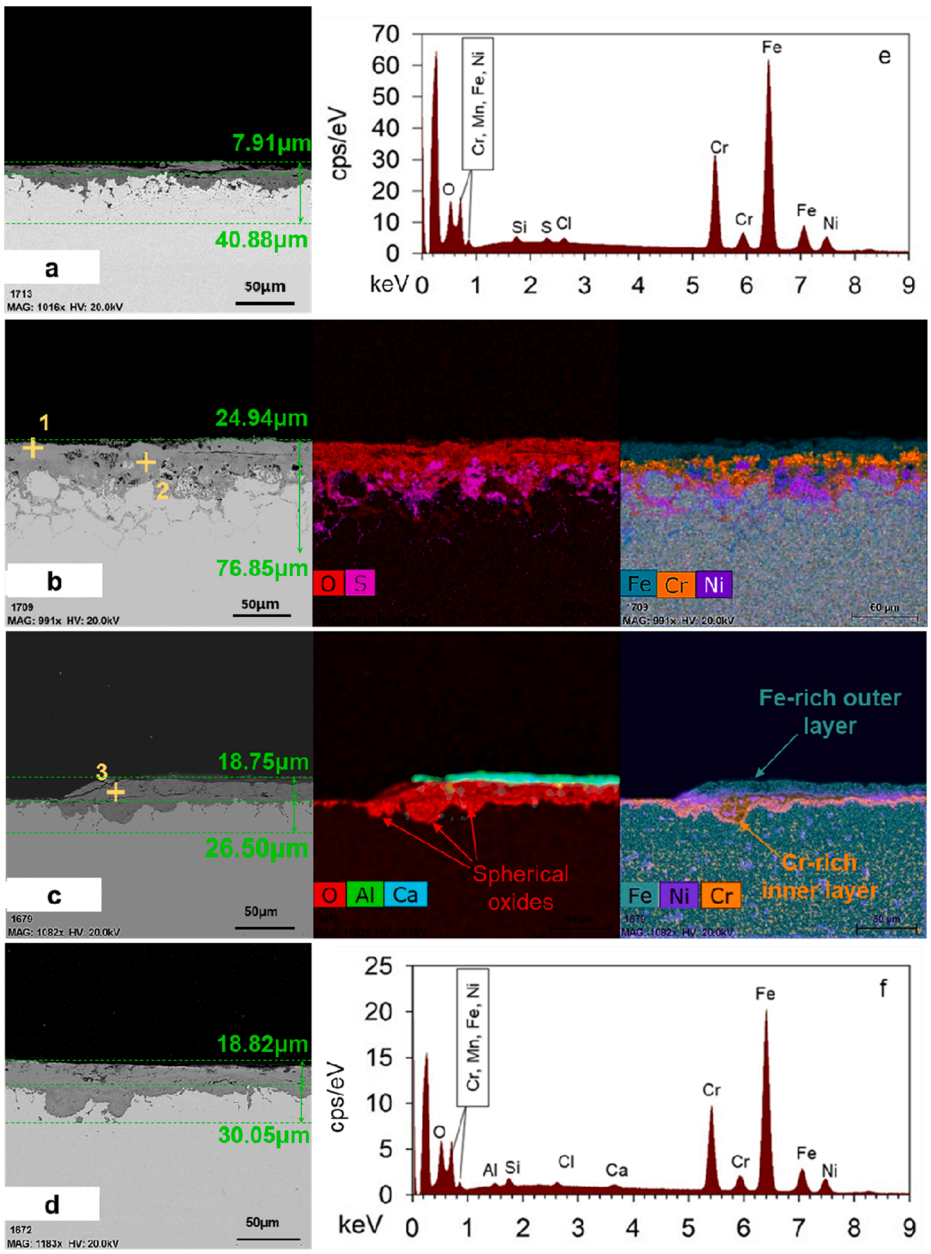

	O	S	Al	Si	Mn	Cr	Fe	Ni
#1	22.5	0.1	0.1	0.5	1.7	2.0	67.0	6.2
#2	16.8	6.0	0.5	0.5	0.4	65.8	8.7	1.3
#3	24.4		0.8	2.0	0.9	2.4	56.7	12.8

Fig. 6. SEM/EDX on the cross-section of the 304 SS substrates: (a) BFB lower position; (b) BFB upper position; (c) CFB 8 m platform; (d) CFB 5 m platform; (e) EDX map spectrum across the corrosions on the BFB upper sample; (f) EDX map spectrum across the corrosions on the CFB 8 m sample; Spot analysis on the corrosion products were conducted [wt%].

3.2. Corrosion of the 304 stainless steel

Fig. 4 shows the phase analysis of both the remaining scales and the exposing areas of the 304 stainless steel specimens after the tests. As seen, the corrosion of the 304 SS was mainly attributed to the substrate oxidation forming Fe_2O_3 and Fe_3O_4 on the surface. Regarding the two samples installed in the BFB rig, a minor fraction (based on the semi-quantification by the software MAUD using ICSD library) of K_2SO_4 and Al/Fe could be identified on the upper sample surface while Fe/Cr/Ni/C (304 SS) and Fe/Ni could only be detected on the lower one. The difference between the XRD results indicates that: (1) at the upper position, the K-bearing fly ash interacted with the 304 SS and the Al/Fe alloy [30] was present due to the Al attack from the fuel as well as the sand particles; (2) at the lower position with the higher local temperature, Fe/Ni was detected due to the oxides spallation. Moreover, the bed particles collision onto the substrate could brush off the ash deposits and the iron oxides, exposing the 304 SS substrate (Fe/Cr/Ni/C). When it comes to the CFB-tested 304 SS samples, major corrosion products (Fe_2O_3 and Fe_3O_4) similar to those formed on the BFB samples were identified. Besides, the calcium aluminium oxide was found on the CFB

samples due to the Al-rich fly ash (Table 1) attack during the corrosion development. Sodium calcium aluminosilicates were detected on the 5 m platform sample. This was attributed to the anthracite inherent Na, Ca contents forming high melting point eutectics with the presence of SiO_2 under the local fuel combustion temperature after a long period of operation.

Fig. 5 shows the surface elemental mapping of selected 304 SS samples focusing on the ash deposits. According to Fig. 5a, on the surface of the BFB upper 304 SS, the ash deposits were dominated by K (identified as K_2SO_4 in Fig. 4) with the presence of Mg and Ca compounds. The K_2SO_4 deposit could be regarded as the initial slagging layer due to the condensation of the aerosol K_2SO_4 to molten and then to solid phase on the substrate surface through reaction R1 [31]. It could further react with SiO_2 and forming slags after a certain operation time through reaction R2. On the surface of the 304 SS at the CFB 8 m position (Fig. 5b), instead of K_2SO_4, the scales mainly consisted of calcium aluminosilicates because of the higher Ca content but lower K content in the anthracite ash comparing to those of the biomass fuels (Table 1). Within the ash-derived aluminium rich (and the presence of Na) atmosphere, the Na-Ca-Al-SiO_2 eutectics (Fig. 4) were formed and attached on the sample surface through reactions R3–R5 [32,33].

$$K_2SO_4(aerosol) \rightarrow K_2SO_4(molten) \rightarrow K_2SO_4(s) \quad \text{(R1)}$$

$$K_2SO_4 + nSiO_2 \rightarrow K_2O \cdot nSiO_2 + SO_3 \quad \text{(R2)}$$

$$Na_2SO_4 + Al_2O_3 + 2SiO_2 \rightarrow 2NaAlSiO_4 + SO_3 \ \text{(Eutectics}\cdots\text{)} \quad \text{(R3)}$$

$$2CaSO_4 + 2Al_2O_3 + 4SiO_2 \rightarrow 2CaAl_2Si_2O_8 + 2SO_2 + O_2 \quad \text{(R4)}$$

$$2Na_2SO_4 + CaSiO_3 + 2SiO_2 \rightarrow Na_4CaSi_3O_9 + SO_2 + O_2 \ \text{(Eutectics}\cdots\text{)} \quad \text{(R5)}$$

The corrosion products could further diffuse into the substrate and therefore the cross-section scanning under SEM is of great importance to verify the corrosion rate. A thin layer of corrosion products of ca.8 μm could be observed above the BFB lower substrate (Fig. 6a) with an oxidation intrusion of ca. 41 μm, while thick multi-layered oxides (ca.25 μm) was observed on the BFB upper substrate (Fig. 6b). The EDX mapping and spot analysis revealed that the outer layer was rich in Fe (spot #1), and the inner layer was mainly Cr-rich oxides (spot #2). Furthermore, the thicker oxides layer led to a deeper diffusion up to ca.77 μm into the substrate with a dichotomous structure dominating by S and Ni. With regards to the CFB samples, the corrosion products were similar to each other; multi-layered porous oxides with a thickness of ca.19 μm could be observed above the substrates and spherical oxides were formed as the frontier against the substrate (Fig. 6c, d). The EDX mapping illustrates that the spherical oxides comprised of an outer layer of Fe-rich oxide (spot #3) and an inner layer of Cr-rich oxide.

Given that the CFB tests experienced a much longer exposure time than BFB tests, the 304 SS samples' corrosion rate was substantially slower in the CFB tests. The main reasons can be obtained by comparing the EDX spectrums across the corrosion products on the samples installed at BFB upper position (Fig. 6e) and CFB 8 m position (Fig. 6f): (1) as seen, sulphur content was detected only on the BFB sample and dissolved by the substrate forming nickel sulphides [34], thus accelerating the corrosion rate; (2) Ca and Al were found on the CFB sample, covering the corrosion products in the form of calcium aluminosilicates. These ash-derived high melting point eutectics effectively hindered the diffusion of sulphur which slowed down the corrosion development; (3) the Cl content from the fuels could act as a catalyst during the metal oxidation (R6–R8) [35]. This process could be further accelerated by the ash-derived alkali chlorides (R9–R10) [23,36] and their sulphation (R11) [37]. Therefore, with a higher alkali (mainly potassium) content

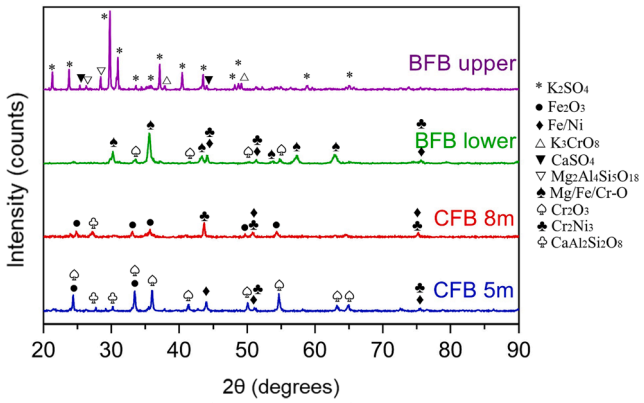

Fig. 7. XRD patterns of the Stellite-6 coating sample surfaces after the test.

in the biomass than anthracite (Table 1) as well as the diffusion of sulphur into the BFB 304 SS, the corrosion rate of the BFB installed samples was much faster than that of the CFB samples.

$$Me(s) + Cl_2(g) \rightarrow MeCl_2(s) \rightarrow MeCl_2(g) \quad \text{(R6)}$$

$$3MeCl_2(g) + 2O_2 \rightarrow M_3O_4 + 3Cl_2(g) \quad \text{(R7)}$$

$$2MeCl_2(g) + \frac{3}{2}O_2 \rightarrow M_2O_3 + 2Cl_2(g) \quad \text{(R8)}$$

where *Me* represents Fe, Cr and Ni R8

$$Cr_2O_3 + 4MaCl(s) + \frac{5}{2}O_2 \rightarrow 2Ma_2CrO_4(s,l) + 2Cl_2(g) \quad \text{(R9)}$$

$$Fe_2O_3 + 2MaCl(s) + \frac{1}{2}O_2 \rightarrow 2MaFeO_2(s,l) + 2Cl_2(g) \quad \text{(R10)}$$

$$2MaCl(s,l,g) + SO_2(g) + \frac{1}{2}O_2(g) \rightarrow Ma_2SO_4(s,l) + 2Cl_2(g) \quad \text{(R11)}$$

where *Ma* represents K and Na R11

3.3. Corrosion behaviour of Stellite-6

According to the XRD results (Fig. 7) of the Stellite-6 coating surfaces, K_2SO_4 deposited on the surface of the BFB upper Stellite-6 sample alongside with magnesium aluminosilicates. The Stellite-6 coating was oxidised, forming K_2CrO_4. With the presence of H_2O_2 and OH^- radicals, K_2CrO_4 can be further oxidised into K_3CrO_8 [38]. At the lower position in the BFB, the corrosion of the coating was mainly done by the alloy oxidation forming Cr_2O_3. Magnesium also participated in the surface oxidation process resulting in Mg/Fe/Cr oxides. On the surfaces of the CFB Stellite-6 specimens, the 8 m platform sample was covered by Cr_2Ni_3 and Fe_2O_3, while Cr_2O_3 appeared to be the main corrosion product of the Stellite-6 located at the 5 m platform with the sintered eutectics of calcium aluminosilicates.

Fig. 8 shows the surface morphology of the Stellite-6 samples under SEM/EDX. A big difference can be observed between the two samples' surfaces located in the BFB combustor. The BFB lower Stellite-6 sample (Fig. 8a) showed a relatively condensed surface with a limited area of sintered fly ash attachment. However, on the BFB upper Stellite-6 sample surface (Fig. 8b), fly ash fusion took place and covered the coating by the molten phase K, Ca, Al, Mg compounds. As explained in the previous section, the widely accumulated fly ash sintering on the upper sample was due to the densified fly ash formation in the freeboard

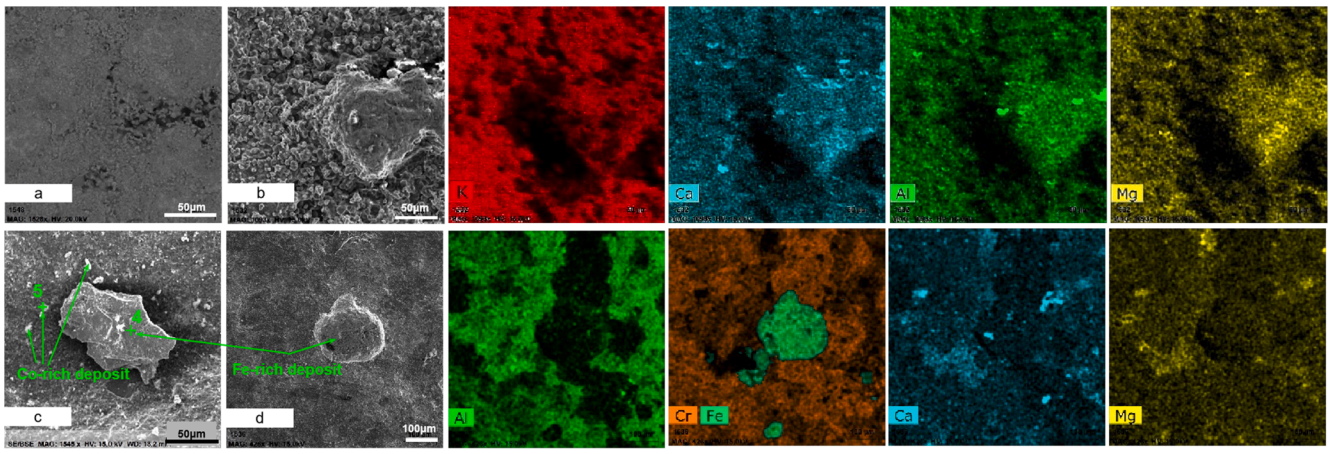

	O	Mg	Al	Si	Ca	Cr	Fe	Co
#4	19.2	-	0.1	-	-	1.4	79.3	-
#5	24.2	1.2	7.7	5.5	2.2	7.0	-	52.3

Fig. 8. SEM images of the Stellite-6 coating surfaces with elemental mapping of selective areas: (a) BFB lower position; (b) BFB upper position; (c) CFB 8 m platform; (d) CFB 5 m platform. Spot analyses on the attached particles were detected [wt%].

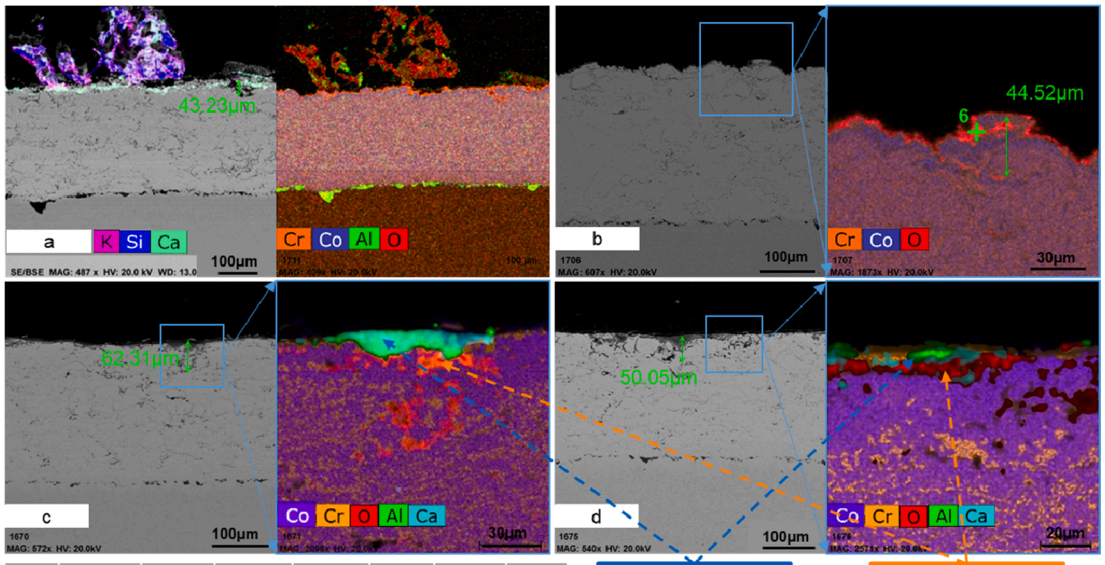

	O	S	Cl	Cr	Fe	Co	W
#6	26.6	-	0.1	60.2	0.6	10.9	1.7

Fig. 9. SEM/EDX on the cross-section of the Stellite-6 coatings: (a) BFB lower position; (b) BFB upper position; (c) CFB 8 m platform; (d) CFB 5 m platform. Spot elemental quantification on the corrosion products was detected [wt%].

zone, and the lower coating sample was vulnerable to self-oxidation because of the bed material collision. In addition, the molten fly ash accumulation on the BFB upper Stellite-6 sample indicates the coating was effectively interdicting the corrosion process comparing to the 304 SS covered by K_2SO_4 deposits with exposed iron oxides (Fig. 5a). However, the molten phase ash can further capture the fine bed particles to form a slagging layer, which may significantly affect the thermal conduction efficiency in practical application of the Stellite-6.

Regarding the two CFB Stellite-6 coating samples (Fig. 8c, d), the surface morphology is similar to each other as the corrosion was mainly formed by coating oxidation (Fe_2O_3, Cr_2O_3, etc.). The ash derived Al and Fe could be detected on the coating surface but there were barely any alkali and alkaline earth metals. This was resulted from the much lower content of K in the anthracite ash, which is the main source of the low melting point eutectics. Moreover, instead of molten ash observed on the BFB Stellite-6 surfaces, ash deposits were found on the CFB samples. The deposits can be generally classified as the attachment of large (>100 μm) Fe-rich particles (Fig. 8 #4) and fine (<10 μm) Co-rich particles (Fig. 8 #5). Considering the relatively long exposure time (ca.1630 h), the presence of some ash deposits was expected but no sign of melting indicates the Stellite-6 coating offered excellent slagging and corrosion protection to the substrates in the CFB set-up.

Fig. 9 shows the SEM/EDX scanning on the cross-sections of the post-test Stellite-6 coatings. They all have dark areas on the interface between the substrate and the coating, which were the artefacts from grit-blasting by alumina. On the outermost surface of the two BFB installed Stellite-6 coatings (Fig. 9a, b), a much thinner layer of metal oxidation (mainly Cr_2O_3, spot #6) can be observed comparing to those of the 304 SS

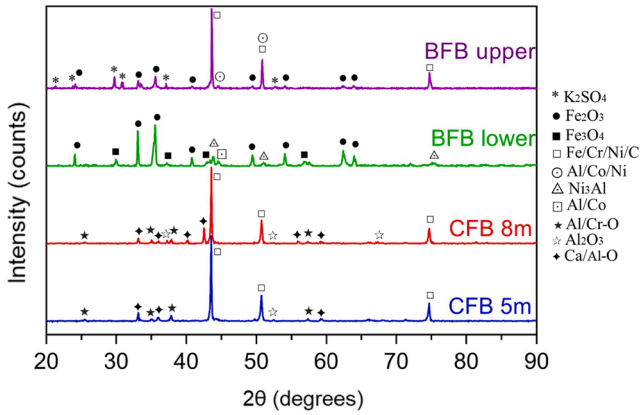

Fig. 10. XRD patterns of the NiAl coating sample surfaces after the test.

specimens. Moreover, for the four specimens, the penetration of the oxides into the coating (marked with green arrows) was only found at certain spots alongside the outer surface due to the chlorine attack through the coating defects or grain boundaries. This can be attributed to the Co-rich layer beneath the very outer Cr-rich layer. As reported by Luthra [39], the formation of the spinel $CoCr_2O_4$ can suppress the chlorine diffusion by introducing cobalt oxide (CoO).

An interesting spot was found on the BFB lower Stellite-6 surface (Fig. 9a), where a bed agglomerate was attached. The agglomeration mechanisms were reported in our previous study [28], and the main compositions of the agglomerates are K, Ca and Si. More importantly, the interface between the attached agglomerate and the coating surface was dominated by Ca.

As it has been discussed, potassium can participate in the corrosion process via R9 and R10. However, it was not detected at the outer layer of the coating indicating the priority of Ca over K during the interaction with the Cr_2O_3 via R12 [40]. Moreover, the resultant $CaCr_2O_4$ can further react with the fly ash derived alumina via R13 [40], and forming stable calcium aluminosilicates as the very outer layer (Fig. 9c, d). This outer layer can cover the corroded Cr hence increase the corrosion resistance of the Stellite-6 coating. As a result, none of the substrates suffered from corrosion because of the protection of Stellite-6.

$$CaO + Cr_2O_3 \rightarrow CaCr_2O_4 \qquad \Delta G_{850^\circ C} = -6.98E + 04J \tag{R12}$$

$$CaCr_2O_4 + Al_2O_3 + SiO_2 \rightarrow CaAl_2SiO_6 + Cr_2O_3 \qquad \Delta G_{850^\circ C} = -2.36E + 04J \tag{R13}$$

3.4. Corrosion performance of NiAl coating

The surface XRD identification (Fig. 10) of the NiAl samples revealed the iron oxidation as the main corrosion product of the BFB lower sample. Clear peaks of the 304 SS substrate (Fe/Cr/Ni/C) were found on the BFB upper sample but not on the lower sample. It is reasonable to infer that the NiAl coating spallation could firstly take place on the BFB lower sample leading to a longer exposure time for the oxidation process of the substrate comparing to that of the BFB upper sample. Furthermore, on the upper BFB specimen, K_2SO_4 was detected as the main scale with the formation of Fe/Ni. Nevertheless, at the lower installation point, Fe_3O_4 was detected as the corrosion product after a longer exposure time due to the earlier coating spallation.

The CFB derived samples showed a similar major phase of Fe/Cr/Ni/C due to the NiAl coating spallation. However, it is not consistent with the observations in Fig. 4, as the exposed 304 SS substrate should be further oxidised and forming Fe_2O_3 and Fe_3O_4 considering the extensively long testing time in the CFB system. According to Fig. 10, the reason could be the formation of the Al_2O_3, Al/Cr-O and Al/Ca-O on the surface. The good thermal stability of these deposits can further protect the substrate from attacking by hot corrosion [41,42].

The edges between the remaining NiAl coating and the substrate were observed under SEM/EDX, and selective areas were shown in Fig. 11. In general, the NiAl coating tested at the BFB upper position (Fig. 11a) had an amorphous surface, and a base could be observed at the edge of the original NiAl coating. However, the CFB 8 m NiAl coating (Fig. 11c) showed a flat surface with the exposure of inner NiAl coating material close to the spallation edge. Meanwhile, no base layer was observed between the coating's edges. The elemental mapping of the spallation edge was performed on larger magnification level to highlight the changes of the NiAl coating and substrate. As shown in Fig. 11b, the original NiAl coating successfully hindered the biomass ash-derived K_2SO_4 attachment which was found on the surface of the 304 SS (Fig. 5a) and Stellite-6 (Fig. 8b) samples. Such observation demonstrates the anti-slagging ability of the NiAl coating. Regarding the exposed substrates after coating spallation, there was very little K, Ca scales on the substrate surfaces. However, the edge between the remaining NiAl coating and the substrate provided a reservoir for the K_2SO_4 accumulation, thereby forming of a base layer (Fig. 11). Arguments might be raised as the accumulated K_2SO_4 can react with the 304 SS substrate. In fact, it can be seen in Fig. 12a that the corrosion was developed in the

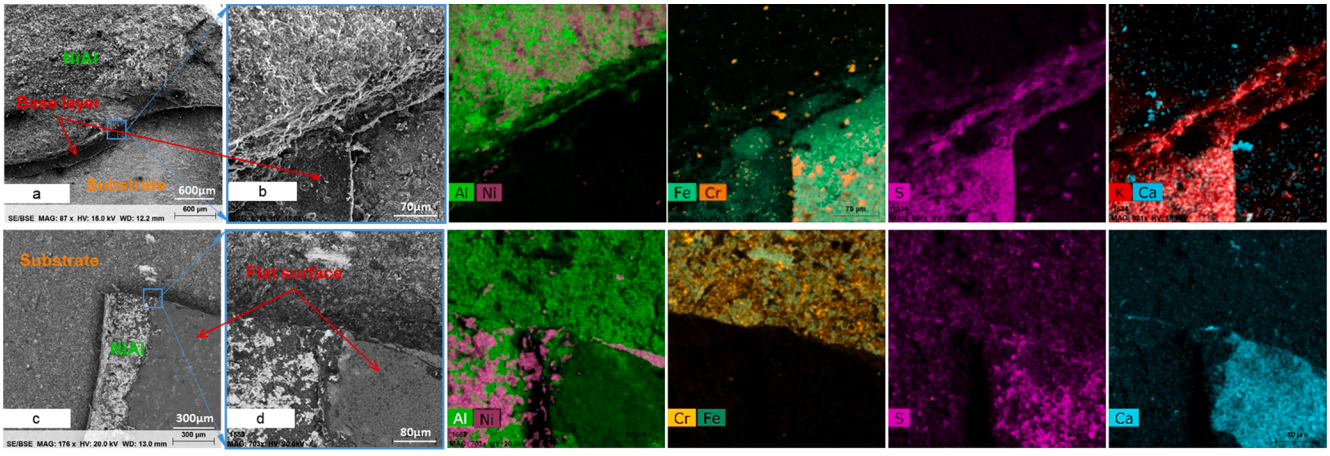

Fig. 11. SEM images of the NiAl coating spallation areas with elemental mapping of selective specimens: (a) General BFB upper NiAl; (b) Magnified BFB upper NiAl with elemental mapping; (c) General CFB 8 m NiAl; (d) Magnified CFB 8 m NiAl with elemental mapping.

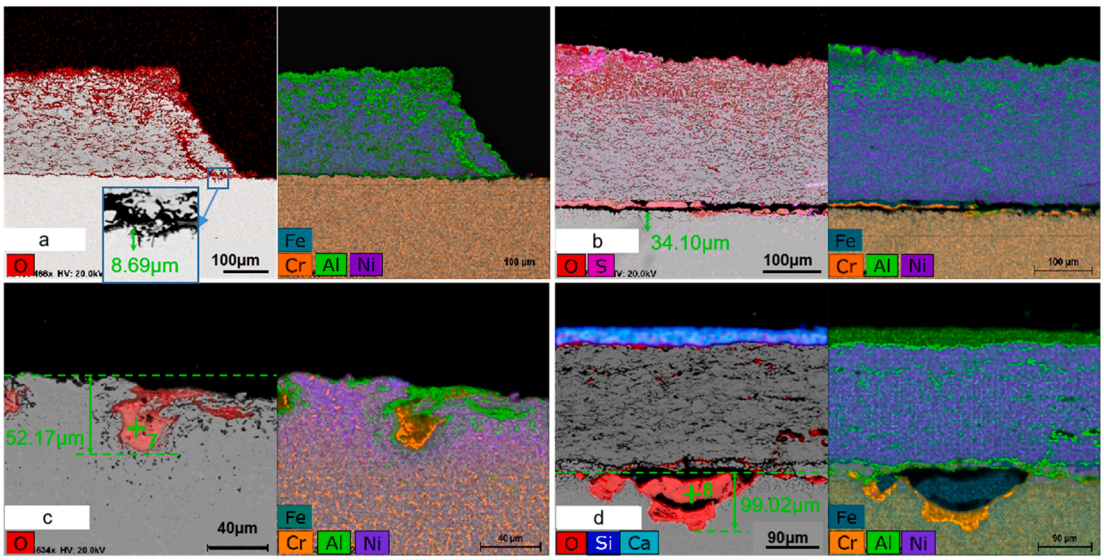

	O	Al	Cr	Mn	Fe	Ni
#7	28.3	2.44	53.7	1.2	4.4	9.3
#8	23.4	-	3.1	1.5	68.2	3.7

Fig. 12. SEM/EDX on the cross-section of the NiAl coatings: (a) BFB lower position; (b) BFB upper position; (c) CFB 5 m platform; (d) CFB 8 m platform. Spot elemental quantification on the corrosion area was conducted [wt%].

substrate at the spalled coating edge and a crack was developed in the NiAl coating starting at the bottom of the coating edge. But under the operation conditions, the attachment of fly ash is a continuous process. Even after shutting down the combustion, the remaining fly ash in the combustor and freeboard can be captured by this edge. Thus, K_2SO_4 could be observed at the surface of the base layer. It would be a very interesting perspective to further investigate the corrosion development at the coating spallation edge. It is also worth noting that the substrate surfaces of the CFB specimens were covered by Al (Fig. 11d) which was identified as Al_2O_3 in Fig. 10. As discussed previously, the formation of the outer Al_2O_3 layer can prevent the Cl penetration. Therefore, the formation of iron oxides (Fe_2O_3 and Fe_3O_4) was restricted. When it comes to the surfaces of the remaining NiAl coatings, flatter surfaces can be observed on the CFB samples (Fig. 11c, d) in comparison to those installed in the BFB (Fig. 11a, b). This was mainly caused by the Ca-rich deposits according to the elemental mapping results.

The cross-section SEM/EDX analysis was conducted on the remaining NiAl coatings, and on account of the full spallation of the NiAl on the CFB 5 m sample, the scanning was focused on its substrate (Fig. 12). On the BFB samples, the growth of alumina started at the coating surface, forming an Al-rich layer and developed across the whole NiAl coating, resulting in the thin Al_2O_3 layer at the bottom of the coating under the chlorine attack. Once a thin and coherent layer of Al_2O_3 forms on the alloy surface with a thickness of only a few hundred nanometers can provide certain oxidation protection. However, for HVOF coatings which have rough surface and porosity, this would induce internal oxidation [43]. As a result, the coherent layer of Al_2O_3 can be damaged. As shown in Fig. 12 a, b, d, a thin layer of Al_2O_3 has been formed at the coating surface but internal oxidation could still take place. The specimen in Fig. 12c lost the cover of NiAl coating and under the collision of bed materials the surface was damaged leaving no continuous Al_2O_3. Consequently, the substrate of the BFB lower sample was corroded with a depth of ca. 9 μm (Fig. 12a) and a 34 μm corrosion depth was developed in the BFB upper substrate (Fig. 12b). These proved the protectiveness of NiAl coating against corrosion comparing to the corrosion of the plain substrate (Fig. 6a, b). Surprisingly, the oxidation of the CFB installed samples reached a depth up to ca. 52 μm (Fig. 12c, no NiAl left on the substrate) and 99 μm (Fig. 12d) in their substrates. In addition, the spherical oxidations were very similar to those observed on the plain 304 SS specimens (Fig. 6c, d) with Cr-rich (spot #7) and Fe-rich (spot #8) layers. However, the oxidation depths of the NiAl coated substrates in CFB should be less than those of the plain 304 SS specimens. The reasons could be: (1) the damage of the substrate during the spray of the coating as NiAl was much more difficult to be coated than Stellite-6. Impurities (pores, foreign bodies such as grits) at the interface can be introduced during coating process or even the grit blasting process prior to the coatings process to roughen the surface so that residual grits might be retained causing the formation of large impurity or even promote the internal oxidation. (2) The severe spherical oxidations were only observed at the two certain spots (Fig. 12c, d) in the NiAl coated substrates unlike those developed across the 304 SS surface. The deeper oxidation spots could be the largest deformation spots during the NiAl coating spallation, which enhanced the development of the corrosion in the substrate. However, further investigations are needed to clarify this observation.

$$NiAl(s) + Cl_2(g) + \frac{3}{4}O_2(g) \rightarrow NiCl_2(s) + \frac{1}{2}Al_2O_3(s) \quad \Delta G_{850^\circ C} = -2.77E + 06J \tag{R14}$$

$$NiCl_2(s) \rightarrow NiCl_2(g) \tag{R15}$$

As mentioned earlier, the rapid penetration of Cl_2 (or Cl^- ion) can accelerate the metal oxidation. Thus, the corrosion of the NiAl could follow the reaction R14 [24]. Likewise, the continuous loss of $NiCl_2$(g) via R15 also accelerated the formation of Al_2O_3 until a coherent Al_2O_3 scale covered the coating alloy, which can effectively hinder the evaporation of $NiCl_2$ and prevent further chlorine attack. This explains the formation of the outer Al-rich layer on the coatings derived from the BFB tests (Fig. 12a, b). However, the distribution of Ni and Al was rather homogeneous across the coating alloy after the CFB tests (Fig. 12d). The main reason was the high Al content (Al_2O_3) in the anthracite ash which can attach on the NiAl coating surface as a protective layer.

Furthermore, the anthracite ash derived Ca and Si can also cover the coating surface in the form of calcium-silicates or react with the Al-rich layer to form calcium aluminosilicates. These high melting point Ca-Al-Si compounds could ultimately protect the coating alloy from corrosion attack, which was not observed on the BFB samples though.

The discussion above reveals the formation of the Al_2O_3 layer at the coating/substrate interface. However, the previous work was carried out in a horizontal tube furnace and the interaction between deposits and coating remained static at a controlled temperature. In this study, the coating samples were placed in semi-pilot scale BFB and industrial CFB which had more complex conditions including not only the fly ash deposition but also bed collision and local temperature variations. Thus, the unexpected NiAl spallation was observed and the possible pathways are: (1) the fast oxidation of the Al in the coating alloy under the chlorine penetration; (2) Al oxidation developed across the coating alloy and reached the coating/substrate interface; (3) cracks were formed in the coating alloy and at the interface after experiencing fluctuated local temperature; (4) the NiAl coating partially spalled off under the collision of the bed materials. Then a coating edge (Fig. 12a) was developed, which facilitated the corrosion propagation into the coating alloy hence promoted the coating spallation. Moreover, on the BFB samples, the coating edge was in favour of capturing the gaseous/molten phase K_2SO_4, which further accelerated the corrosion development at the coating/substrate interface.

4. Conclusions

The corrosion resistance of Stellite-6 and NiAl coatings has been investigated in a lab-scale biomass fuelled BFB combustor and an industrial scale CFB boiler firing anthracite. The two coatings were deposited via high velocity oxy-fuel (HVOF) onto 304 stainless steel substrates which were installed at different heights alongside the BFB combustor and CFB boiler. Comparing to the corrosion on the plain substrates, the following conclusions can be drawn:

- The 304 stainless steel corroded much faster in the biomass-fired BFB (up to 77 μm in 20 h) compared to the anthracite-fuelled CFB (up to 30 μm in 1630 h). This was due to the enhancement of the chlorine-induced corrosion by the higher K content in the biomass ash comparing to the anthracite ash. Moreover, the abundant Al content in the anthracite ash formed the outermost Al_2O_3 dense layer which further restrained the corrosion development.
- The corrosion attack was limited at certain spots on the Stellite-6 coating surfaces. The depth of the corrosion reached up to 45 μm and 63 μm in the coatings located in BFB and CFB respectively, but no corrosion was observed on the substrates in all Stellite-6 coated specimens. The successful protection of the substrates was attributed to the formation of the Cr_2O_3 outer layer and the sub-layer rich in Co ($CoCr_2O_4$ and CoO).
- Most of the NiAl coatings spalled off the substrates after the tests. This was due to the oxides penetrating through the coating and forming the Al_2O_3 layer at the coating/substrate layer which separated the coating from the substrate under the collision of the bed particles. Even with the remaining NiAl coating, the corrosion propagated into the substrates reaching a depth up to 34 μm and 99 μm in the BFB and CFB samples respectively. Although the Al-rich anthracite ash promoted the formation of the protective Al_2O_3 layer at the outermost surface, the NiAl coating spalled off after certain time in the CFB setup.

The results of this study indicate that the Stellite-6 coating is a superior anti-corrosion material for combustion of biomass and anthracite in fluidised bed systems. NiAl coating has certain corrosion resistance, but when exposed to the bed particle collision, it may suffer from fatal failure of spallation, which needs to be considered for application in real fluidised bed boilers.

Data availability statement

The raw/processed data required to reproduce these findings cannot be shared at this time due to technical or time limitations.

CRediT authorship contribution statement

Hetian Chi: Investigation, Formal analysis, Writing - original draft, Writing - review & editing. **Miguel A. Pans:** Investigation, Writing - review & editing. **Mingwen Bai:** Investigation, Writing - review & editing. **Chenggong Sun:** Methodology, Writing - review & editing, Supervision, Funding acquisition. **Tanvir Hussain:** Methodology, Writing - review & editing, Supervision, Funding acquisition. **Wei Sun:** Methodology, Writing - review & editing, Supervision, Funding acquisition. **Yuge Yao:** Investigation. **Junfu Lyu:** Methodology, Supervision, Project administration. **Hao Liu:** Conceptualization, Methodology, Writing - review & editing, Supervision, Funding acquisition, Project administration.

Declaration of Competing Interest

The authors declare that they have no known competing financial interests or personal relationships that could have appeared to influence the work reported in this paper.

Acknowledgements

This work was supported by the UK Engineering and Physical Sciences Research Council [grant number EP/M01536X/1].

The authors acknowledge Dr. Huan Liu from Huazhong University of Science and Technology for the coal sample characterisations. The authors would also like to thank Mr. Tony Gospel for manufacturing the sampling probes and the Lihua Starch Co. Ltd. for the experimental assistance with the industrial CFB boiler tests.

The authors thank the Nanoscale and Microscale Research Centre (nmRC) for providing access to instrumentation.

Appendix

Table A.1
PDF card number of the phases identified by XRD.

Phases	PDF card number
K_2SO_4	00-044-1414
Fe_2O_3	00-024-0072
Al/Fe	00-039-0824
Fe_3O_4	01-075-0033
Fe/Cr/Ni/C	00-033-0397
Fe/Ni	00-012-0736
$CaAl_4O_7$	00-046-1475
Na-Ca-Al-SiO_4	00-003-0499
K_3CrO_8	01-075-1032
$CaSO_4$	00-037-0184
$Mg_2Al_4Si_5O_{18}$	00-012-0235
Mg/Fe/Cr-O	01-071-1254
Cr_2O_3	00-038-1479
Cr_2Ni_3	03-065-6291
$CaAl_2Si_2O_8$	00-005-0528
Al/Co/Ni	00-046-1062
Ni_3Al	03-065-6613
Al/Co	00-050-0786
Al/Cr-O	01-077-2188
Al_2O_3	00-001-1308
Ca/Al-O	00-032-0148

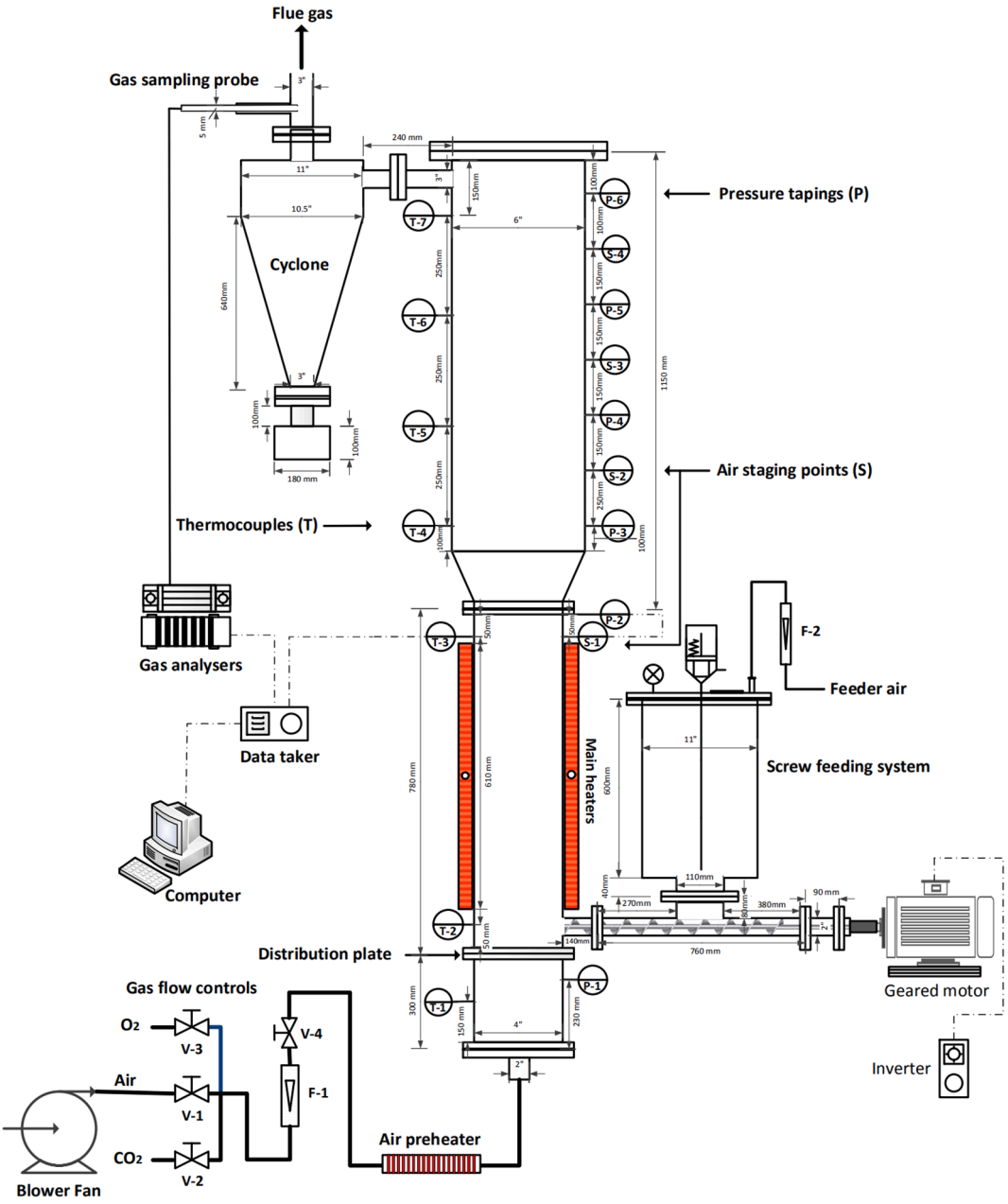

Fig. A1. Schematics of the 20kWth bubbling fluidised bed.

20kWth bubbling fluidised bed combustor- design and operational conditions

Operational conditions: The fluidisation air, 15 m^3/hr at ambient temperature and atmospheric pressure (ATAP) is supplied from a compressor, heated up by an electric pre-heater before the plenum, and then fed into the combustor through a porous stainless gas distribution plate (100 μm pore size and 12 mm thickness). Two electric half-cylindrical ceramic radiant heaters around the combustion zone are used to preheat the air flow and the bed particles during the start-up of the combustor. The combustor is equipped with pressure tapings and sheathed K-type thermocouples at different heights, and the measurements of temperatures and the pressure drop across the bed are continuously recorded with a datataker system. Once the bed temperature reaches about 500 °C, biomass pellets are fed into the combustor at the location just above the distribution plate by a screw feeder (frequency controlled). To prevent back firing, an extra air flow of 5.7 m^3/hr (ATAP), which also stops the sand coming into the fuel feeding pipe, is fed through the feeding hopper. Therefore in this study, a total air flow of 20.7 m^3/hr (ATAP) is supplied for the combustion purposes, and the excess O_2 in the flue gas is controlled between 4 and 5% by maintaining a suitable fixed fuel feeding rate during the test. The combustion bed temperature is controlled at ~ 890 °C due to the safety consideration of the experimental apparatus.

References

[1] Parliament E. Promotion of the use of energy from renewable sources. Amendment 324, Proposal for a directive, Recital 7 2018.
[2] VITO TU Wien, INFRO, Rütter Soceco, PwC UU. Sustainable and optimal use of biomass for energy in the EU beyond 2020. European Commission: 2017.
[3] Centre JR. Brief on biomass for energy in the European Union. European Commission: 2019.
[4] Lauri P, Havlík P, Kindermann G, Forsell N, Böttcher H, Obersteiner M. Woody biomass energy potential in 2050. Energy Policy 2014;66:19–31.

[5] Khan AA, de Jong W, Jansens PJ, Spliethoff H. Biomass combustion in fluidized bed boilers: Potential problems and remedies. Fuel Process Technol 2009;90(1):21–50.
[6] Grabke HJ, Reese E, Spiegel M. The effects of chlorides, hydrogen chloride, and sulfur dioxide in the oxidation of steels below deposits. Corros Sci 1995;37(7):1023–43.
[7] Lyu J, Yang H, Ling W, Nie L, Yue G, Li R, et al. Development of a supercritical and an ultra-supercritical circulating fluidized bed boiler. Frontiers in Energy 2019;13:114–9.
[8] Demirbas A. Potential applications of renewable energy sources, biomass combustion problems in boiler power systems and combustion related environmental issues. Prog Energy Combust Sci 2005;31(2):171–92.
[9] Fukuda Y. Development of Advanced Ultra Supercritical Fossil Power Plants in Japan: Materials and High Temperature Corrosion Properties. Materials Science Forum 2011;696:236–41.
[10] Sidhu TS, Agrawal RD, Prakash S. Hot corrosion of some superalloys and role of high-velocity oxy-fuel spray coatings—a review. Surf Coat Technol 2005;198(1-3):441–6.
[11] Kaur M, Singh H, Prakash S. A survey of the literature on the use of high velocity oxy-fuel spray technology for high temperature corrosion and erosion-corrosion resistant coatings. Anti-Corrosion Meth Material 2008;55(2):86–96.
[12] Oksa M, Tuurna S, Varis T. Increased lifetime for biomass and waste to energy power plant boilers with HVOF coatings: high temperature corrosion testing under chlorine-containing molten salt. J Therm Spray Tech 2013;22(5):783–96.
[13] Hack H, Stanko GS. Update on Fireside Corrosion Resistance of Advanced Materials for Ultra-Supercritical Coal-Fired Power Plants. In: The 31st International Technical Conference on Coal Utilization & Fuel Systems; 2006. p. 21–5.
[14] Phalnikar CA, Evans EB, Baldwin WM. High temperature scaling of cobalt-chromium alloys. J Electrochem Soc 1956;103(8):429. https://doi.org/10.1149/1.2430374.
[15] Sidhu TS, Prakash S, Agrawal RD. Hot corrosion studies of HVOF NiCrBSi and Stellite-6 coatings on a Ni-based superalloy in an actual industrial environment of a coal fired boiler. Surf Coat Technol 2006;201(3-4):1602–12.
[16] Pettersson C, Pettersson J, Asteman H, Svensson J-E, Johansson L-G. KCl-induced high temperature corrosion of the austenitic Fe–Cr–Ni alloys 304L and Sanicro 28 at 600°C. Corros Sci 2006;48(6):1368–78.
[17] Li YS, Niu Y, Wu WT. Accelerated corrosion of pure Fe, Ni, Cr and several Fe-based alloys induced by ZnCl2–KCl at 450°C in oxidizing environment. Mater Sci Eng, A 2003;345(1-2):64–71.
[18] Li YS, Spiegel M, Shimada S. Effect of Al/Si addition on KCl induced corrosion of 9% Cr steel. Mater Lett 2004;58(29):3787–91.
[19] Asteman H, Spiegel M. A comparison of the oxidation behaviours of Al2O3 formers and Cr2O3 formers at 700°C – Oxide solid solutions acting as a template for nucleation. Corros Sci 2008;50(6):1734–43.
[20] Israelsson N, Engkvist J, Hellström K, Halvarsson M, Svensson J-E, Johansson L-G. KCl-Induced Corrosion of an FeCrAl Alloy at 600 °C in O2 + H2O Environment: The Effect of Pre-oxidation. Oxid Met 2015;83(1-2):29–53.
[21] Israelsson N, Unocic KA, Hellström K, Jonsson T, Norell M, Svensson J-E, Johansson L-G. A Microstructural and Kinetic Investigation of the KCl-Induced Corrosion of an FeCrAl Alloy at 600 °C. Oxid Met 2015;84(1-2):105–27.
[22] Oksa M, Auerkari P, Salonen J, Varis T. Nickel-based HVOF coatings promoting high temperature corrosion resistance of biomass-fired power plant boilers. Fuel Process Technol 2014;125:236–45.
[23] Li YS, Spiegel M, Shimada S. Corrosion behaviour of various model alloys with NaCl–KCl coating. Mater Chem Phys 2005;93(1):217–23.
[24] Bai M, Reddy L, Hussain T. Experimental and thermodynamic investigations on the chlorine-induced corrosion of HVOF thermal sprayed NiAl coatings and 304 stainless steels at 700 °C. Corros Sci 2018;135:147–57.
[25] Hjörnhede A, Sotkovszki P, Nylund A. Erosion-corrosion of laser and thermally deposited coatings exposed in fluidised bed combustion plants. Mater Corros 2006;57(4):307–22.
[26] Yu S, Zhang J, Cheng J. Carbon reduction cost estimating of Chinese coal-fired power generation units: A perspective from national energy consumption standard. J Cleaner Prod 2016;139:612–21.
[27] Pala Z, Bai M, Lukac F, Hussain T. Laser Clad and HVOF-Sprayed Stellite 6 Coating in Chlorine-Rich Environment with KCl at 700 °C. Oxid Met 2017;88(5-6):749–71.
[28] Chi H, Pans MA, Sun C, Liu H. An investigation of lime addition to fuel as a countermeasure to bed agglomeration for the combustion of non-woody biomass fuels in a 20kWth bubbling fluidised bed combustor. Fuel 2019;240:349–61.
[29] Sher F, Pans MA, Afilaka DT, Sun C, Liu H. Experimental investigation of woody and non-woody biomass combustion in a bubbling fluidised bed combustor focusing on gaseous emissions and temperature profiles. Energy 2017;141:2069–80.
[30] Fadeeva VI, Leonov AV. Amorphization and crystallization of Al-Fe alloys by mechanical alloying. Mater Sci Eng, A 1996;206(1):90–4.
[31] Niu Y, Zhu Y, Tan H, Hui S, Jing Z, Xu W. Investigations on biomass slagging in utility boiler: Criterion numbers and slagging growth mechanisms. Fuel Process Technol 2014;128:499–508.
[32] Niu Y, Du W, Tan H, Xu W, Liu Y, Xiong Y, Hui S. Further study on biomass ash characteristics at elevated ashing temperatures: The evolution of K, Cl, S and the ash fusion characteristics. Bioresour Technol 2013;129:642–5.
[33] Zhang B, Zhong Z, Xue Z, Xue J, Xu Y. Release and transformation of potassium in co-combustion of coal and wheat straw in a BFB reactor. Appl Therm Eng 2018;144:1010–6.
[34] Dravnieks A. Kinetics of Nickel-Sulfur and Steel-Sulfur Reactions. J. Electrochem. Soc. 1955;102(8):435. https://doi.org/10.1149/1.2430120.
[35] Lehmusto J, Yrjas P, Skrifvars B-J, Hupa M. High temperature corrosion of superheater steels by KCl and K2CO3 under dry and wet conditions. Fuel Process Technol 2012;104:253–64.
[36] Li YS, Niu Y, Spiegel M. High temperature interaction of Al/Si-modified Fe–Cr alloys with KCl. Corros Sci 2007;49(4):1799–815.
[37] Metsäjoki J, Huttunen-Saarivirta E, Lepistö T. Elevated-temperature corrosion of uncoated and aluminized 9–12% Cr boiler steels beneath KCl deposit. Fuel 2014;133:173–81.
[38] Shi X, Dalal NS. Evidence for a fenton-type mechanism for the generation of .OH radicals in the reduction of Cr(VI) in cellular media. Arch Biochem Biophys 1990;281(1):90–5.
[39] Luthra KL. Kinetics of the Low Temperature Hot Corrosion of Co-Cr-Al Alloys. J. Electrochem. Soc. 1985;132(6):1293–8. https://doi.org/10.1149/1.2114105.
[40] Hu H, Shi M, Yang Y, Liu H, Xu M, Shen J, Yao H. Further Insight into the Formation and Oxidation of CaCr 2 O 4 during Solid Fuel Combustion. Environ. Sci. Technol. 2018;52(4):2385–91.
[41] Nath M, Ghosh A, Tripathi HS. Hot corrosion behavior of Al 2 O 3 –Cr 2 O 3 refractory by molten glass at 1200 °C under static condition. Corros Sci 2016;102:153–60.
[42] Wang X, Zhao P, Chen J, Zhao H, He K. Corrosion resistance of Al–Cr-slag containing chromium–corundum refractories to slags with different basicity. Ceram Int 2018;44(11):12162–8.
[43] Muthu SM, M A. Investigations of hot corrosion resistance of HVOF coated Fe based superalloy A-286 in simulated gas turbine environment. Eng Fail Anal 2020;107:104224.